Available online at www.sciencedirect.com
SCIENCE DIRECT®
Journal of Theoretical Biology 227 (2004) 103–120
Journal of Theoretical Biology
www.elsevier.com/locate/jtbi

Critical conditions for pattern formation and in vitro tubulogenesis driven by cellular traction fields

Patrick Namy, Jacques Ohayon, Philippe Tracqui*

Equipe Dynacell, Laboratoire TIMC-IMAG, CNRS UMR 5525, Institut de l'Ingénierie et de l'Information de Santé (In³s), F-38706 La Tronche cedex, France

Received 27 March 2003; received in revised form 19 September 2003; accepted 7 October 2003

Abstract

In vitro angiogenesis assays have shown that tubulogenesis of endothelial cells within biogels, like collagen or fibrin gels, only appears for a critical range of experimental parameter values. These experiments have enabled us to develop and validate a theoretical model in which mechanical interactions of endothelial cells with extracellular matrix influence both active cell migration—haptotaxis—and cellular traction forces. Depending on the number of cells, cell motility and biogel rheological properties, various 2D endothelial patterns can be generated, from non-connected stripe patterns to fully connected networks, which mimic the spatial organization of capillary structures. The model quantitatively and qualitatively reproduces the range of critical values of cell densities and fibrin concentrations for which these cell networks are experimentally observed. We illustrate how cell motility is associated to the self-enhancement of the local traction fields exerted within the biogel in order to produce a pre-patterning of this matrix and subsequent formation of tubular structures, above critical thresholds corresponding to bifurcation points of the mathematical model. The dynamics of this morphogenetic process is discussed in the light of videomicroscopy time lapse sequences of endothelial cells (EAhy926 line) in fibrin gels. Our modeling approach also explains how the progressive appearance and morphology of the cellular networks are modified by gradients of extracellular matrix thickness.

Keywords: Angiogenesis modeling; Endothelial cell network; Cellular traction; Biogel; Biomechanical instabilities; Bifurcation; Finite element method

1. Introduction

In many physiological and pathological processes, including wound healing, placental development, solid tumor growth or inflammation, formation of new capillaries from pre-existing vasculature plays a crucial role. It is largely recognized that this morphogenetic branching process, globally defined as angiogenesis, is in fact a rather complicated and highly regulated multi-factorial process (Vailhe et al., 1997; Cines et al., 1998; Ingber, 2002). It begins in vivo with the degradation of the extracellular matrix (ECM) and subsequent dispersion of endothelial cells (EC) which also acquire the ability to migrate toward angiogenic stimuli. Cell proliferation and their subsequent association in tube-like structures (tubulogenesis) give rise to the lumen of new capillaries, while tube interconnections and anastomoses define the building topology of the new capillary network (Folkman and Haudenschild, 1980). EC cultured on biogel can mimic this morphogenetic process, and thus provide experimental models allowing progressive investigations of both the large number of biological factors involved in the different phases, and, more importantly, of the different ways these factors interplay (Ingber, 2002).

Angiogenic factors can be roughly divided into soluble (mainly cytokines and a large number of peptides) and insoluble substances (Sage and Vernon, 1994). Stimulation of cell motility by growth factors such as vascular endothelial growth factor (VEGF) is well documented (Roman and Weinstein, 2000), with recent emphasis on possible agonistic effects on the cell response depending on VEGF spatial distribution (Gerhardt et al., 2003). Chemotactic cell response

*Corresponding author. Tel.: +33-476-549-486; fax: +33-476-549-549.
E-mail address: philippe.tracqui@imag.fr (P. Tracqui).

0022-5193/$ - see front matter © 2003 Elsevier Ltd. All rights reserved.
doi:10.1016/j.jtbi.2003.10.015

induced by such diffusible growth factors is still largely considered as a fundamental mechanism for vascular network formation. However, the increasing recognition of mechanical forces as key regulators of cell function has significantly enlarged the chemotactic paradigm by taking into account the determinant role of mechanical coupling between endothelial cells and ECM in tubulogenesis. Indeed, many cell functions such as migration, proliferation and adhesion are influenced by the biomechanical context (Lambert et al., 2001) and an increasing amount of data has established that bi-directional cell–ECM signaling depends on the balance between the traction exerted by the cells and the passive mechanical resistance of the ECM to these cellular forces (Ingber, 2002; Jamora and Fuchs, 2002). In the context of in vitro angiogenesis, videomicroscopy imaging has provided a clear and direct evidence of the mechanical stresses undergone by the ECM: spatial reorganization of EC, seeded on a fibrin matrix, is correlated to an increasing dilatation of ECM areas progressively depleted of fibrin, the lacunae (Vailhe et al., 1997). These lacunae both increase in size and number, leading to a complete remodeling of the matrix into a scaffold which would define the underlying architecture of the capillary network (Fig. 1).

In recent years, different mathematical models have been developed to describe in vitro angiogenesis experiments with direct consideration of insoluble angiogenic factors (Sherratt et al., 1993; Anderson and Chaplain, 1998; Sherratt and Chaplain, 2001; Levine et al., 2001). Anderson and Chaplain (1998) have modeled tumor-induced angiogenesis when cells respond to the haptotactic signal given by the fibronectin they secreted. More recently, Levine et al. (2001) have considered detailed biochemical interactions between EC and extracellular substances, and have simulated the creation of one pseudocapillary structure, but without considering the overall formation of a capillary network. However, even if these models can simulate EC network formation on rigid substrate coated with ECM proteins, they cannot explain morphogenesis of cellular network observed on thick biogels. To overcome these limitations, continuum models have been developed in the conceptual framework defined by Murray and Oster (1984): they explicited the mechanical interactions between cells and a viscoelastic ECM, with special emphasis on the morphogenetic role played by cellular traction forces (Manoussaki et al., 1996; Olsen et al., 1998; Murray et al., 1998; Holmes and Sleeman, 2000; Tranqui and Tracqui, 2000). Considering that such mechanical interactions are of primary importance during in vitro angiogenesis, Manoussaki et al. (1996) and Murray et al. (1998) proposed a 2D model, essentially mechanical, which successfully reproduces the heterogeneous spatial distribution of cell density observed during in vitro angiogenesis. Our paper extends this approach by considering how the formation of cell networks is influenced by the coupling between haptotactic cell migration along ECM gradients, and the spatial distribution of the cell traction, which induces strain fields within the matrix. Indeed, we expect that the relationship between active cell migration and cell traction forces could initiate or prevent the development of the angiogenesis process. Recently, Shreiber et al. (2003) demonstrated that different migration–traction relationships can be exhibited during the compaction of biogel by fibroblasts, with either positive or negative correlation of cell migration to traction. In our paper, we investigate the importance of the balance between the rigidity of the extracellular adhesive support, the contractility tone of endothelial cell cytoskeleton and active cell migration as a critical step for capillary tube formation in vitro. We consider three possible controls of the ECM on the migration–traction relationships. The first one is a modulation of the cell migration by the ECM thickness. The second one is based on the possible long-range mechanical effects due to the fibrous nature of the ECM and the third one assumes that random cell

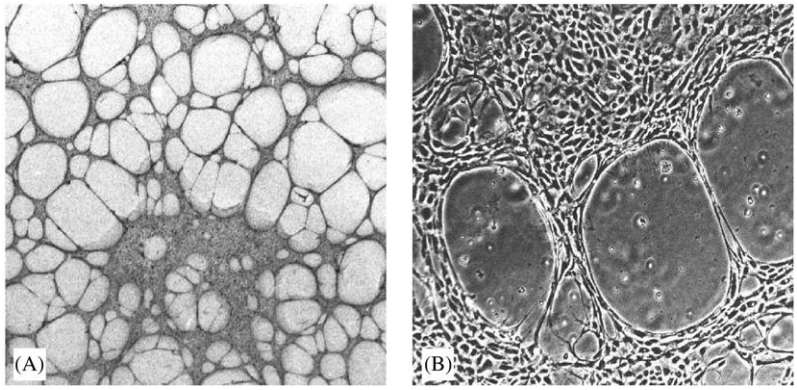

Fig. 1. Morphology of the free upper surface of the fibrin gels remodeled by HUVEC seeded 20 h before. (A) The formation of the capillary-like cellular network (grey areas) surrounding gel lacunae (white areas) is clearly visible (image size: 10 mm × 10 mm). (B) Enlargement of the cell–ECM composite scaffold around areas devoided of fibrin, the lacunae (phase-contrast microscopy, image size: 1 mm × 1 mm).

migration can be biased by the time varying strain field within the ECM.

Our aim is to demonstrate that this theoretical model can explain, for biophysically admissible parameter values, a whole set of experimental results conducted on fibrin biogels, and which have established that networks of tube-like cellular structures only appear for a precise range of controlled experimental parameters. Thus, model validation will be qualitatively and quantitatively discussed with regard to the tubulogenesis inhibition observed when the density of seeded cells increases, or when the stiffness of the ECM is increased. The less rigid the extracellular support, the more EC switched to a tubular network distribution (Vailhe et al., 1997; Tranqui and Tracqui, 2000; Deroanne et al., 2001).

In the first part of the paper, we derive theoretical bifurcation conditions that can be related to the critical experimental threshold beyond which a spatial pre-patterning of the fibrin gel can be generated. From this theoretical analysis, a finite element approach has been used to simulate the nonlinear dynamical behavior of the biomechanical model. We then investigated how EC spatial organization is controlled dynamically within the fibrin gel, the biogel patterning appearing as a pre-requisite scaffold for the formation of subsequent endothelial tube networks. Special attention has been paid to the model parameter values, derived from the quantification of cell traction forces (Tranquillo et al., 1992; Ferrenq et al., 1997) and the rheological analysis of fibrin gels with different fibrin concentrations and stiffness (Benkherourou et al., 2000). We finally discuss the length and time-scales of the biogel pre-patterning process, as well as the influence of geometrical features such as the ECM thickness on the tubulogenesis morphogenetic process.

2. Experimental approach

Experiments conducted with fibrin gels are of specific interest, since fibrin is a constitutive element of ECM, which is involved in wound healing, tumor invasion (Hayen et al., 1999; Van Hinsbergh et al., 2001), and in the elaboration of biomaterials (Grassl et al., 2002). Experimental results reported here are obtained with fibrin gels with 1 mm thickness, following the experimental protocol described in Vailhe et al. (1998). Briefly, 1 ml of fibrinogen solutions at concentrations varying between 0.5 and 4 mg/ml were mixed in sterile 35 mm diameter Petri dishes with Ca^{2+}/Mg^{2+} free PBS 1X, thrombin (0.4 U/ml) and aprotinin (5 μg/ml), an inhibitor of proteases, which is used to control the fibrin gel degradation. Fibrin gels were allowed to polymerize overnight at 37°C in a humidified atmosphere and were used during the following day. In vitro assays were performed with a permanent EC line, EAhy926, derived from the fusion of human umbilical vein endothelial cells (HUVEC) with a carcinoma cell line. Varying cell densities, typically 1.5×10^5 cells suspended in 1 ml of medium containing antibiotics, were then seeded on the fibrin gels.

Lacunae and cell network formation were observed under phase contrast with an Axiovert 135M inverted light microscope (Zeiss Achrostigmat 5×0.12) equipped with a temperature-controlled stage and an incubation chamber (37°C, 5% CO_2, 90% hygrometry) (Carl Zeiss, Germany). The spatio-temporal dynamics of cell networks was recorded using a cooled CCD camera CoolSNAP (Photometrics®/Roper Scientific), allowing low light level detection and short exposure times.

3. Biomechanical modeling of in vitro angiogenesis

We model the fibrin gel as a linear viscoelastic continuous medium, submitted to the coupling between (i) an active cell migration against the ECM gradient induced by EC traction forces on one hand, (ii) the increasing level of cellular stresses with increasing ECM density on the other hand. The interplay of both phenomena generates a mechanical autocatalytic-like process, which is analysed by considering a minimal three-variable differential system: $n(\mathbf{x}, t)$ denotes the EC density at spatial position $\mathbf{x}$ at time t, $\rho(\mathbf{x}, t)$ is the ECM density at spatial position $\mathbf{x}$ at time t, and $\mathbf{u}(\mathbf{x}, t)$ is the displacement vector of the ECM from its original to its deformed position. If $\mathbf{x}_0$ and $\mathbf{x}_1$ are the original and displaced position of a point on the ECM, respectively, the corresponding displacement vector at time t is $\mathbf{u}(\mathbf{x}_0, t) = \mathbf{x}_1 - \mathbf{x}_0$.

3.1. Active and passive stresses within the ECM

The mechanical interactions between EC and ECM mainly result from the balance between the active traction stress generated by EC, and the passive resisting viscoelastic stresses developed by the ECM in response to this mechanical stimulation.

3.1.1. Cell traction stress

Adherent cells can exert substantial traction forces upon the surrounding tissue or matrix thanks to specific adhesion sites (Balaban et al., 2001). At the macroscopic level, cell traction forces are assumed to be (i) proportional to the gel density (Delvoye et al., 1991; Barocas et al., 1995) and (ii) bounded at high cell density due to inhibition contact phenomenon and competition for ECM binding sites (Moon and Tranquillo, 1993; Ferrenq et al., 1997). Thus, we consider that cell traction stresses can be modeled by the following stress

tensor:

$$\boldsymbol{\sigma}_{cell} = \tau\rho n(N_2 - n)\mathbf{Id}, \quad (1)$$

where the parameter τ monitors the individual cellular traction amplitude, related to the cell contractility tone. The real positive constant N_2 ($N_2 > n$) controls the cell traction inhibition when cell density increases, and **Id** is the identity tensor.

3.1.2. Constitutive relationships describing the ECM rheology

We assume that the constitutive stress–strain relationship describing the viscoelasticity of the ECM is given by adding elastic stresses, $\boldsymbol{\sigma}_{ecm}^{elastic}$, proportional to strains, and viscous stresses, $\boldsymbol{\sigma}_{ecm}^{viscous}$, proportional to strain rates (Fung, 1993; Murray, 2003a).

$$\boldsymbol{\sigma}_{ecm} = \boldsymbol{\sigma}_{ecm}^{viscous} + \boldsymbol{\sigma}_{ecm}^{elastic}.$$

The formulation of the $\boldsymbol{\sigma}_{ecm}^{elastic}$ stress tensor is based on linear elasticity. Moreover, we have considered that the fibrous nature of the ECM may induce non-local mechanical effects since fibers can transmit elastic stress between points in the ECM that are quite far apart.

The first component of the elastic stress tensor is given by the Hooke's law

$$\boldsymbol{\sigma}_{linear\ \ elasticity} = \frac{E}{1+v}\left[\boldsymbol{\varepsilon} + \frac{v}{1-2v}\,\theta\,\mathbf{Id}\right].$$

Long-range elastic effects have been modeled by considering second-order terms in the elastic stress tensor (Cruywagen et al., 1997; Murray, 2003a):

$$\boldsymbol{\sigma}_{long\text{-}range\ \ elasticity} = \frac{E}{1+v}\left[-\beta_1\nabla^2\boldsymbol{\varepsilon} - \frac{v}{1-2v}\,\beta_2\nabla^2\theta\,\mathbf{Id}\right].$$

In these formulae, $\boldsymbol{\varepsilon}$ is the strain tensor $\left(\boldsymbol{\varepsilon} = \frac{1}{2}(\nabla\mathbf{u} + \nabla\mathbf{u}^{\mathrm{T}})\right)$, E is the Young's modulus, v the Poisson ratio, β_1 and β_2 are the long-range elastic coefficients (β_1 are β_2 nonnegative constants, in m^2 unit), θ is the dilatation ($\theta = \nabla.\mathbf{u}$) and **Id** is the identity tensor. As it will be shown in the model theoretical analysis, such long-range effects can stabilize the ECM spatial inhomogeneous patterns which can be observed beyond some bifurcation thresholds.

Combining linear and long-range elasticity, we obtain the following expression of the elastic stress tensor:

$$\boldsymbol{\sigma}_{ecm}^{elastic} = \boldsymbol{\sigma}_{linear\ \ elasticity} + \boldsymbol{\sigma}_{long\text{-}range\ \ elasticity}. \quad (2)$$

The viscous component of the ECM stress tensor is also defined in a linear framework, with viscous stress being proportional to the rate of change of the ECM strain tensor $\boldsymbol{\varepsilon}$.

$$\boldsymbol{\sigma}_{ecm}^{viscous} = \mu_1\frac{\partial\boldsymbol{\varepsilon}}{\partial t} + \mu_2\frac{\partial\theta}{\partial t}\mathbf{Id},$$

where μ_1 and μ_2 are the shear and bulk viscosities, respectively.

3.2. Endothelial cell migration equation

Cell migration is a multifactorial process, which is exceedingly difficult to model. Indeed, we have to deal with both molecular-level cell properties and population-level cell function, where individual cell parameters (translocation speed, adhesion strength) are reflected in cell population parameters (random motility or diffusion coefficient, chemotaxis/chemokinesis coefficients, haptotaxis/haptokinesis coefficients) (Maheshwari and Lauffenburger, 1998). However, our working hypothesis is that the modeling of cell population migration behavior by macroscopic fluxes should shed light on how cell migration operate, in conjunction with cellular traction, to drive the tubulogenesis process. As stated in the "Introduction" section, we will focus here on mechanically driven cell migration (mechanotaxis) rather than on a more involved chemotactic scenario. This is justified by our experimental model (obvious mechanical forces, no source of chemoattractant if compared to in vitro angiogenesis induced by tumor-released growth factors) and our wish to explain the tubulogenesis process by a minimal three-variable model (i.e. without considering chemoattractant concentration as a fourth variable). Focusing on mechanical control of cell migration is even reinforced by considering that the expression and secretion of chemoattractant, such as VEGF, can be increased by mechanical factors such as cell stretch (Warner and Mitchell, 2003; Yoshino et al., 2003).

In our modeling of cell migration, the random dispersal of cells down a cell density gradient, i.e. cell diffusion, is counterbalanced by cell migration up an adhesive extracellular gradients (haptotaxis), assumed proportional to the gradient of matrix density generated by cell traction forces. The haptotactic flux J_h is thus given by

$$\mathbf{J}_h = hn\nabla\boldsymbol{\rho},$$

where h is the haptotactic coefficient. Indeed, cells can get a stronger grip on ECM regions with higher number of adhesion sites, resulting in a bimodal variation of the migration speed when binding site density is increased (Palecek et al., 1997).

Another well-documented component of cell mechanotaxis is the migration by contact guidance, where the extracellular substrate defines preferred directions for cell locomotion (Barocas and Tranquillo, 1997; Girton et al., 2002). In particular, Korff and Augustin (1999) performed angiogenesis experiments on a pre-stressed ECM and quantified the extent of anisotropic cell migration in vitro. These results will be used here as the experimental counterpart of our analysis of strain-dependent diffusion based on the theoretical approach developed by Cook (1995) to account for ECM fiber orientation. He proposed to modify the usual expression

of isotropic cell diffusion by considering a strain-biased random walk of cells described by the following diffusive flux:

$$\mathbf{J}_d = -\nabla.(\mathbf{D}(\boldsymbol{\varepsilon})n),$$

where $\mathbf{D}(\boldsymbol{\varepsilon})$ is a strain-biased diffusion tensor.

Expansion of this strain-dependent diffusive flux gives: $\mathbf{J}_d = -\mathbf{D}(\boldsymbol{\varepsilon})\nabla n - n\nabla.[\mathbf{D}(\boldsymbol{\varepsilon})]$ which provides an additional term, compared to the usual expression $\mathbf{J}_d = -\mathbf{D}\nabla n$. This relationship can be compared to the particular flux expression derived from the master equation, based on the principles of the reinforced random walk, of Othmer and Stevens (1997): they called it a "chemotactic sensitivity" in the case of a chemical-biased diffusion. In our case, this term indicates a mechano-sensitivity. The influence of this additional term on ECM remodeling will be analysed below. Considering all these components of cell migration, cell density variation with time is given by the equation:

rate of change of cell density
= cell convection + cell diffusion + cell haptotaxis
+ cell proliferation − cell death.

Typical cell proliferation doubling time is in the order of 30 h for EAhy926 cells, and thus cell proliferation can be neglected in the first stage of the tubulogenesis process. Observations of the fibrin gel–EC medium also indicate that cell detachment and apoptosis is limited in the experimental time-scale. Thus, the above balance equation reduces to the following conservation equation:

$$\frac{\partial n}{\partial t} + \nabla.[\mathbf{J}_c + \mathbf{J}_d + \mathbf{J}_h] = 0, \tag{3}$$

where $\mathbf{J}_c = n\partial\mathbf{u}/\partial t$ is the passive cell convective flux.

3.3. ECM conservation equation

In addition to the mechanical remodeling, ECM structure and composition can be affected by the matrix proteolysis and the localized secretion of new ECM by the cells. This latter phenomenon is quite difficult to quantify experimentally and requires a specific approach based, for instance, on ECM labeling with fluorescent probes. If ECM biosynthesis can have significant effect on rigid substrate, the amount of newly secreted matrix will remain quite negligible with regard to the existing initial fibrin matrix in our experiments. Furthermore, Vernon et al. (1995) reported that even EC which do not synthesized type-I collagen, were able to reorganize, on a longer time-scale, the ECM and to create a cellular network.

On the other hand, ECM proteolysis, induced by specific proteases, can significantly affect biochemical ECM remodeling. Under these conditions, the spatio-temporal evolution of the ECM density is given by the mass balance equation:

rate of change of ECM density
= convection − degradation.

In order to investigate a minimal possible scenario for the tubulogenesis process, we will however neglect, in our following analysis, the degradation term. This simplification is supported by both experimental and theoretical considerations. Experimentally, ECM degradation can be modulated and prevented by using aprotinin (see "Experimental approach" section), an inhibitor of matrix proteases (Vailhe et al., 1998). Vailhe and his coworkers also measured the time evolution of the concentration of fibrin degradation products during the tubulogenesis process. They showed that fibrin degradation remains very limited when the first lacunae are formed in the biogel. We therefore consider that ECM proteolysis will mostly act as a modulator and as an amplifier of the tubulogenesis process. Theoretically, ECM proteolysis could be taken into account, in a first approximation, by considering a decrease of ECM elastic moduli in a successive quasi-state based approach.

According to the above arguments, we thus consider that the spatio-temporal variation of the ECM density is given by the conservation equation:

$$\frac{\partial \rho}{\partial t} = -\nabla.\left[\rho\frac{\partial \mathbf{u}}{\partial t}\right]. \tag{4}$$

3.4. Reduction of the analysis to a 2D domain

In order to simplify the finite element simulation of our model, we restricted our analysis in a 2D domain by considering first that the fibrin gel geometry in our experiments is a thin plane (1 mm thickness), second that, since cells are seeded on the biogel (and not dispersed during gel polymerization), principal stress component in the vertical direction, σ_{33}, remains negligible. In order to keep a track of the gel thickness variation everywhere in the 2D domain, we then deduce from Hooke's law the following relationship between the gel thickness $e(x, y, t)$ and the local ECM density $\rho(x, y, t)$ (see Appendix A):

$$e(x, y, t) = e_0(x, y)\left(\frac{1-3\nu}{1-2\nu} + \frac{\nu}{1-2\nu}\frac{\rho(x, y, t)}{\rho_0}\right), \tag{5}$$

where $e_0(x, y)$ and $e(x, y, t)$ denote the ECM thickness at time t_0 and t, respectively.

An additional approximation is necessary to take into account the effect of the boundary condition at the bottom of the Petri dish, where the biogel is attached. This boundary condition induces shear stresses which decrease with the matrix thickness. This effect is modeled by introducing, in the force balance equation, an external restoring body force, $\mathbf{R}_{ext}$, which is derived

by evaluating the pure shear stress, σ_{i3}, at $z = e(x, y, t)$. From linear elasticity theory, we get

$$\sigma_{i3}(x, y, t) = \frac{Eu_i(x, y, t)}{(1 + v)e(x, y, t)} \quad i = 1, 2. \tag{6}$$

where u_i is the ith component of the displacement vector $\mathbf{u}$.

Therefore, combining Eqs. (5) and (6), we can model the attachment force to the Petri dish by $\mathbf{R}_{ext} = s\mathbf{u}/\rho$, where s is the restoring elastic parameter depending on the elastic modulus E and the Poisson ratio.

Since, in these experiments, we can ignore all inertial effects compared to viscous effects, we obtain as the final the mechanical balance equation:

$$\nabla.[\boldsymbol{\sigma}_{cell} + \boldsymbol{\sigma}_{ecm}] = \mathbf{R}_{ext}. \tag{7}$$

Combining Eqs. (1), (2) and (7), the force balance equation reads explicitly:

$$\nabla.\left[\frac{E}{1+v}\left(\boldsymbol{\varepsilon} - \beta_1\nabla^2\boldsymbol{\varepsilon} + \frac{v}{1-2v}(\theta - \beta_2\nabla^2\theta)\,\mathbf{Id}\right) + \mu_1\frac{\partial\boldsymbol{\varepsilon}}{\partial t} + \mu_2\frac{\partial\theta}{\partial t}\mathbf{Id} + \tau\rho n(N_2 - n)\,\mathbf{Id}\right] = s\frac{\mathbf{u}}{\rho}. \tag{8}$$

Finally, we have to specify the analytical expression of the 2D-strain dependent diffusion tensor $\mathbf{D}(\boldsymbol{\varepsilon})$, already given in Cook (1995) or in Manoussaki et al. (1996):

$$\mathbf{D}(\boldsymbol{\varepsilon}) = D_0\begin{bmatrix} 1 + \dfrac{\varepsilon_{11} - \varepsilon_{22}}{2} & \dfrac{\varepsilon_{12} + \varepsilon_{21}}{2} \\ \dfrac{\varepsilon_{12} + \varepsilon_{21}}{2} & 1 - \dfrac{\varepsilon_{11} - \varepsilon_{22}}{2} \end{bmatrix},$$

where D_0 is a scalar parameter and ε_{ij} are the strain tensor components.

3.5. Initial and boundary conditions

In vitro angiogenesis experiments are conducted in a Petri dish, assimilated for simplicity to a squared $L \times L$ region Ω with boundary $\partial\Omega$, which is impermeable to cells and ECM. Therefore, boundary conditions are zero-flux ones for the model variables:

$$\mathbf{J}_d^n.\boldsymbol{\eta} = \mathbf{J}_h^n.\boldsymbol{\eta} = \mathbf{J}_c^n.\boldsymbol{\eta} = 0,$$

where $\boldsymbol{\eta}$ is the normal vector of the boundary.

Moreover, since the biogel is stuck to the border of the Petri dish, we prescribe zero displacement on the boundaries ($\mathbf{u}_{|\partial\Omega} = 0$) and no propagation of strains through them ($(\nabla.\boldsymbol{\varepsilon}).\boldsymbol{\eta} = 0$ on $\partial\Omega$). This implies a zero-flux boundary condition for ECM density (see Eq. (4)).

As initial conditions for EC density, we considered is a slightly and randomly perturbed ($\pm 10\%$) spatial distribution around the steady-state value n_0. Additional initial cell distribution profiles will also be considered in the "Results" section. We furthermore assume an homogeneous initial distribution of the ECM density $\rho(\mathbf{x}, 0) = \rho_0$, the biogel being in an undeformed state $\mathbf{u} = \mathbf{0}$.

4. Mechanical instability conditions

We first determine relevant grouping of model parameters by introducing non-dimensionalized variables $(n, \rho, \mathbf{u})$ with associated normalized parameters (see Appendix B). In order to get indications on the critical role played by the leading model parameters, such as cell traction amplitude on the ECM remodeling, a linear stability analysis has been carried out, in a standard way, in a neighborhood of the normalized homogeneous steady state $n = 1$, $\rho = 1$, $\mathbf{u} = \mathbf{0}$. This analysis checks the pattern forming potential of our model and helps to predict parameter ranges for which spatial patterns could emerge from small spatial perturbations. However, as known from the nonlinear dynamical system theory, this analysis is no longer valid when nonlinear terms become dominant and the model solution grows. This approach will thus be completed by a numerical integration of the model equations using a finite element approach. The linearized equations are detailed in Appendix C.

Spatial perturbations are chosen of the particular form $\exp(\mathrm{i}(kx + ly) + \xi(k, l)t)$, where k, l are the spatial wavenumbers in the x and y directions, respectively, and $\xi(k, l)$ is an eigenvalue of the Jacobian matrix of the linearized system. $\xi(k, l)$ determine the growth rate of the corresponding perturbation. The homogeneous steady state is linearly stable if all eigenvalues have a non-positive real part, with perturbations decreasing to zero as t tends to infinity. On the contrary, all spatial perturbations associated with eigenvalue $\xi(k, l)$, with a positive real part, grow exponentially.

Let $r = k^2 + l^2$. After some algebraic manipulations, the dispersion relation can be expressed as a fourth degree polynomial equation of the form

$$\xi(\xi - \xi_1)(a(r)\xi^2 + b(r)\xi + c(r)) = 0, \tag{9}$$

where ξ_1 is an eigenvalue with a negative real part. The dispersion coefficients $a(r)$, $b(r)$ and $c(r)$ are detailed in Appendix C.

Since we are focusing on the mechanical interaction between EC and the ECM, we choose the cell traction amplitude τ as the main bifurcation parameter. In the parameter space, we then derive from the expression of $c(r)$ a necessary and sufficient condition for a saddle–node bifurcation corresponding to a Turing instability (Murray, 2003a). This critical value τ_{turing} of the cell traction amplitude τ is given by

$$\tau_{turing} = \frac{\lambda + 2\mu + 2\sqrt{s(2\mu\beta_1 + \lambda\beta_2)}}{(3N_2/2 - 2) + h/D_0(N_2 - 2)}, \tag{10}$$

where parameter expressions are given in Appendix B.

However, the wavenumbers are of the form of $k = \pi k^*/L$, $l = \pi l^*/L$, where k^* and l^* are integers. Thus, the eigenvalues associated to $r = \pi^2 N/L^2$, $N = k^{*2} + l^{*2}$, are discrete. So, unless the dispersion relation

includes in its range of unstable modes at least one of these discrete values, no structure can develop (Fig. 2).

Let us discuss, from the instability condition (10), the respective influence of cell traction, cell migration and ECM mechanical properties on the onset of lacunae formation within the matrix. The importance of ECM mechanical properties on the ECM homogeneity (no lacunae) or ECM remodeling (creation of lacunae) appears explicitly through this relationship. For supercritical value of τ ($\tau > \tau_{turing}$), a non-uniform steady state of the matrix density can appear, which, according to Eq. (5), corresponds to local changes of the matrix thickness, i.e. to the first stages of the lacunae formation. This is in agreement with the intuition: the more rigid the ECM (increasing value of E, and thus of λ and μ (see Eq. (B.1) in Appendix B)), the larger the cellular traction must be to destabilize the system. Moreover, cell haptotaxis lowers the critical threshold for instability since, in absence of cell haptotactic migration ($h = 0$), a larger cell traction amplitude is required to induce the lacunae formation within the biogel. More globally, condition (10) highlights that the ratio h/D_0 is a key factor for lacunae formation: net cell migration can indeed occur in opposite directions, depending on the balance between haptotaxis and diffusion. Starting from a randomly perturbed but almost homogeneous distribution of cells, one can intuitively imagine how instabilities may be generated: if haptotaxis is large enough compared to diffusion, combination of active cell movement together with mechanical local increase of cell traction forces may initiate an autocatalytic process which is strong enough to overcome the viscoelastic resistance of the ECM. The influence of the other model parameters can be discussed along the same lines. Restoring force coefficient s and material long-range parameters β_1 and β_2 tend to prevent the ECM mechanical remodeling. As expected, ECM remodeling is also controlled by inhibition of cell traction: for a given value of τ corresponding to lacunae formation, decreasing the limiting cell density value will prevent the appearance of a mechanical instability within the matrix.

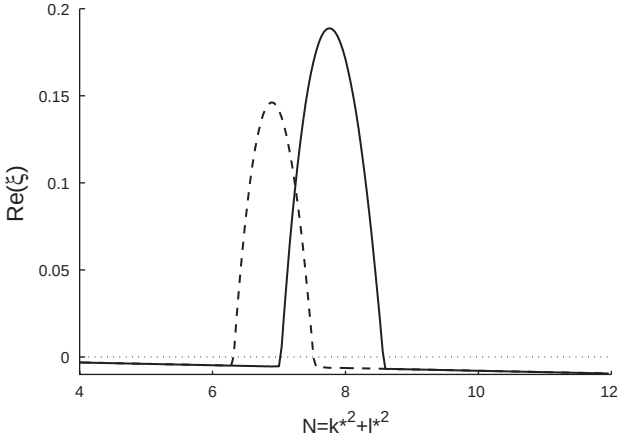

Fig. 2. Stability diagram derived from the model dispersion Eq. (9). The largest real part of eigenvalues is plotted as a function of the sum N of the squared values of the modes k^*, l^* in x and y directions, respectively ($N = k^{*2} + l^{*2}$ with k^*, l^* integers). Unstable modes will appear for N values taken inside the interval defined, on the $\Re(\xi(k,l)) = 0$ axis, by the inner region of the dotted and solid line curves. However, the above equality on N is only satisfied for the solid line curve, with $k^* = l^* = 2$, which corresponds to the mode (2, 2). The solid line curve is obtained with normalized parameters. Normalized parameters used, for the solid line curve, are: $\tau = 2.39$, $\lambda = 1.2$, $\mu = 1.8$, $\mu_1 = \mu_2 = 0.03$, $\beta_1 = \beta_2 = 0.0031$, $D_0 = 8 \times 10^{-5}$, $h = 4 \times 10^{-5}$, $N_2 = 3$, $s = 90$.

However, we already quoted above that the linear stability analysis is no longer valid out of the steady-state neighborhood, i.e. when nonlinear effects intervene. This limitation can be partly overcome by using asymptotic expansion techniques, as developed for a similar but simpler two-variable cell–ECM mechanical model by Cruywagen et al. (1994) and more recently by Piechor and Kazmierczak (2002) for the analysis of traveling wave solutions. The analysis of the model nonlinear dynamical properties presented in the next sections relies on finite element simulations of the ECM remodeling. However, the analytical results obtained by Cruywagen et al. (1997) have been used to validate our numerical approach (see next paragraph).

5. Numerical simulations of the biogel patterning

5.1. Finite element simulations

A finite element method, developed with the Femlab© software, has been used to solve the partial differential equation system (Eq. (B.2) in Appendix B). The 2D square domain is meshed by 1000 nodes and 2500 triangle elements. Numerical integration of the time-dependent problem has been performed with the multi-step Matlab© solver *ode15*. Total conservation of the ECM density and EC concentration were monitored, and different mesh options (number of nodes, number of elements, degree of elements) were used to ensure stability and accuracy of our numerical computations. The validity of numerical approach has been especially checked by simulating the model of Cruywagen et al. (1997), which shares several mathematical similarities with the one presented here. We thus compared successfully our numerical results to the approximated analytical solutions derived from nonlinear bifurcation analysis, in the case of a non-symmetrical mixed mode steady state (Fig. 5 in Cruywagen et al., 1997).

5.2. Mechanical and cell parameter values

Ranges of values of the mechanical parameters of our model are both derived from previous experiments and

Table 1
Range of mechanical parameter values, extracted from literature and considered for the simulations of the mechanocellular model dynamics

Parameter	Numerical range	Units	Reference
Young's modulus E	10^3–10^4	Pa	Benkherourou et al. (2000)
Poisson ratio v	0.15–0.25	—	Scherer et al. (1991) Shreiber et al. (2003)
Shear viscosity μ_1	10^5–10^8	Pa s	Barocas and Tranquillo (1997)
Bulk viscosity μ_2	10^5–10^8	Pa s	Murray et al. (1998) Holmes and Sleeman (2000)
Traction force coefficient τ	10^{-9}–10^{-5}	Pa cm^9/(g cell^2)	Tranquillo et al. (1992) ($\tau = 0.001$ dyn cm^4/(mg cell)) Ferrenq et al. (1997) Shreiber et al. (2003) ($\tau = 0.015$ dyn cm/cell)

Table 2
Range of cell parameter values

Biological features	Numerical range	Units	Reference
Cell diffusion D_0	10^{-9}–10^{-6}	cm^2/s	DiMilla et al. (1992) Barocas et al. (1995)
Cell haptotaxis h	10^{-8}–10^{-5}	cm^2/(s g)	Dickinson and Tranquillo (1993) Perumpanani and Byrne (1999)
Initial cell concentration n_0	0.5×10^5–5×10^5	cell/cm^3	Delvoye et al. (1991); Vailhe et al. (1997) Murray et al. (1998)
Initial gel density ρ_0	0.5–8	mg/cm^3	Delvoye et al. (1991); Vernon et al. (1992) Vailhe et al. (1997)
Cell traction inhibition N_2	2×10^5–2×10^6	cell/cm^3	Ferrenq et al. (1997) Tranqui and Tracqui (2000)

extracted from other publications (Table 1). In addition, Table 2 indicates the estimated range of values for the cell parameters used in the model simulation, with corresponding references.

6. Results

6.1. Qualitative aspects and dynamics of lacunae formation

Simulations of the model dynamical behavior have been performed for different parameter sets taken in the instability domain defined by the linear stability analysis. Preliminary simulations (Fig. 3) illustrate the robustness of the ECM remodeling with regard to different sets of shape of EC initial conditions. Indeed, linear stability analysis cannot predict which spatial patterns will emerge, from unstable mode selections, for different initial conditions on the model variables. In Fig. 3, similar steady-state patterns are obtained, starting from different initial distribution of cells, the initial ECM density being spatially homogeneous ($\rho_0(x, y) = 1$). Thus, ECM remodeling does not result from amplification of initial conditions but really from self-organizing properties of the cell–ECM composite medium.

As a first step in the analysis of the simulation results, we also quantify independently the influence of the strain-biased cell random motility by simulating anisotropic cell diffusion over an elastic medium pre-stressed by uniaxial stretching. Fig. 4 shows that there is a significant directional bias of cell random migration: cell motion increases in the direction of the largest dilatation of the medium, while the mean ratio between the diffusion coefficients in the x and y directions ($D_{11}(\varepsilon)/D_{22}(\varepsilon)$) is in the order of 1.4.

This simulated cell population behavior can be compared to experimental results obtained by Korff and Augustin (1999), who performed cell migration assay on a pre-strained biogel. We computed the same directionality (or shape) index of the cell distribution, defined as the ratio long axis/short axis of the ellipsoid defining iso-levels of cell concentrations (Fig. 5). This figure shows a very good agreement with the experimental index values.

However, we can wonder if this strain-dependent diffusion still remains significant when it is replaced in the global cell migration context defined by our model. We thus we carried out simulations of the complete model without (Fig. 6A) or with (Fig. 6B) a strain-biased diffusion. We found that, for conditions leading to ECM mechanical remodeling, the amplitude of the strain field within the ECM is too weak to influence

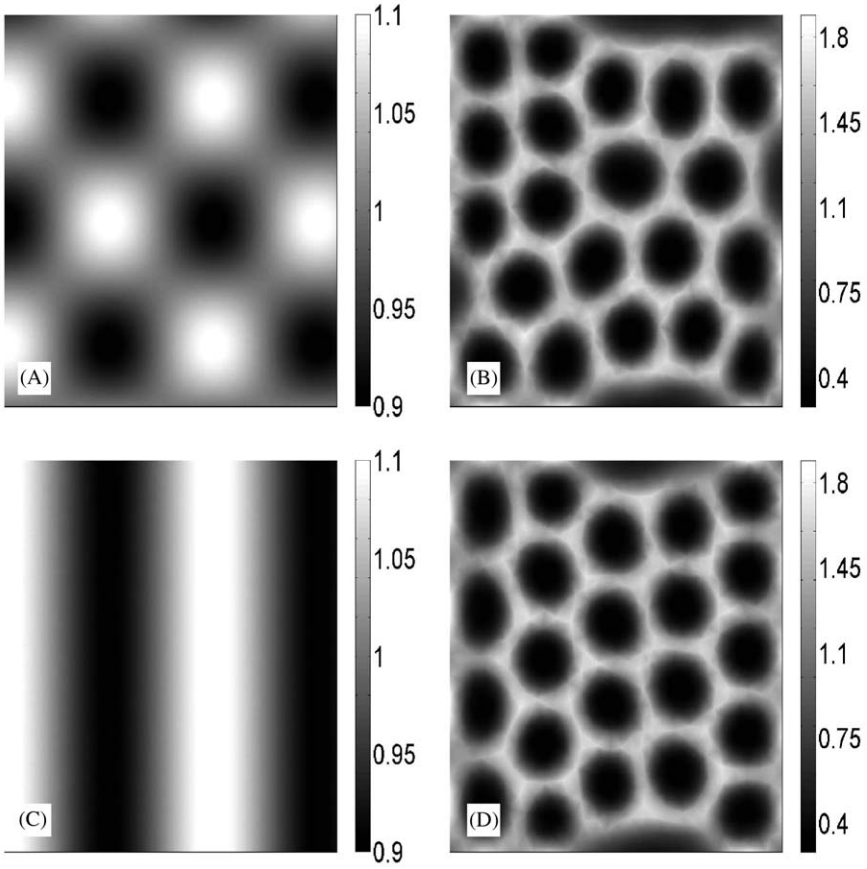

Fig. 3. Steady-state ECM patterns obtained, starting from the same initial total amount of cells but which are distributed according to different spatial profiles (A, C). After a transient phase, both cell distributions give nearly the same ECM remodeling pattern (B, D). Normalized parameters used were: $\tau = 3.41$, $\lambda = 0.15$, $\mu = 0.23$, $\mu_1 = \mu_2 = 0.003$, $\beta_1 = \beta_2 = 0.01$, $D_0 = 8 \times 10^{-6}$, $h = 4 \times 10^{-5}$, $N_2 = 2.72$, $s = 8800$. Scales indicate the normalized EC density.

qualitatively the tubulogenesis process (the mean ratio between the diffusion coefficients, defined above, is in this case in the order of 1.01). However, lacunae geometry seems to be more precisely defined in the strain-dependent diffusion case, with larger values of cell densities occurring along the ECM cords. Similar conclusions were obtained with the model of Manoussaki et al. (1996) and Murray et al. (1998), i.e. without counterbalancing cell diffusion by haptotactic cell migration. Thus, strain-dependent cell diffusion does not appear essential for the tubulogenesis process.

6.2. Comparison with in vitro experiments

According to EC type and fibrin concentration, significant differences in time-scales have been reported for the development of in vitro tubulogenesis (Vernon et al., 1992; Vailhe et al., 1998, 2001). For HUVEC cultured on fibrin gel, lacunae appear typically in less than 2 h while cellular network formation is achieved after 24 h. Sizes of lacunae range from 0.2 to 1.5 mm. For Bovine Retinal Endothelial Cell (BREC), 46 h are needed to observe the formation of capillary-like networks. Thanks to our theoretical analysis, we succeed in finding experimentally based parameter values which lead to simulations of lacunae formation with time and spatial scales in agreement with experimental ones. Simulated lacunae appear within 12 h with morphology and network organization very similar to the experimental observations (Fig. 7).

Fig. 8 shows the associated progressive formation of lacunae along a cross-section of the ECM, the matrix thickness being computed from Eq. (5).

Starting from this first level of model validation, we carried on a refined confrontation of the model properties with a larger body of experimental data, considering different bifurcation parameters for the onset of the mechanically induced instability leading to capillary-like structure formation.

6.2.1. Critical threshold of seeded endothelial cells concentration

Thanks to the stability analysis, we can predict, for given rheological properties of the fibrin gel, the EC

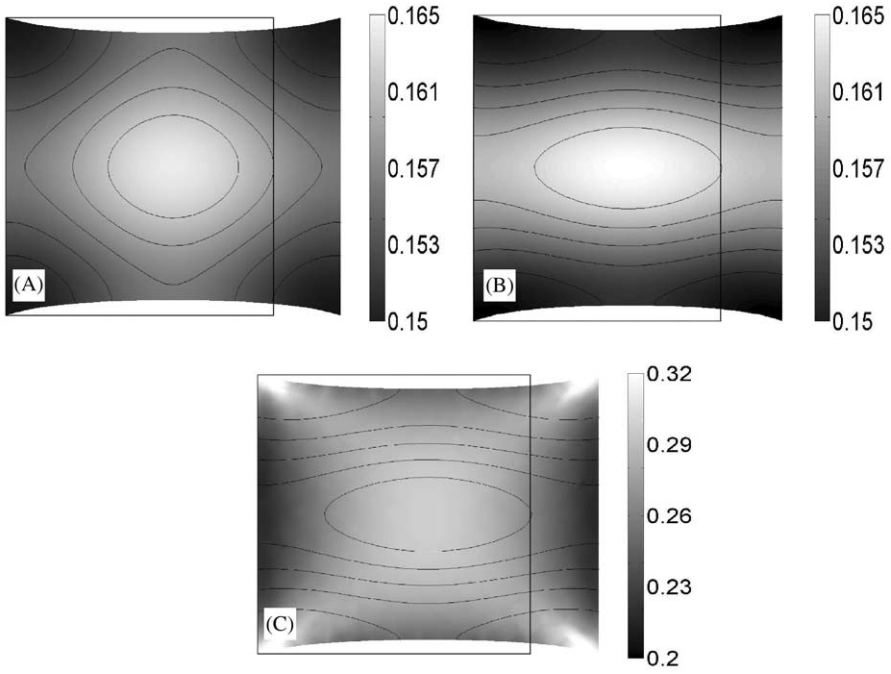

Fig. 4. Influence of ECM mechanical strains on cell random migration. Cell diffusion on a stretched elastic medium obeys either to the classical Fick's law with constant diffusion coefficient (A) or is controlled by a strain-dependant diffusion tensor $\mathbf{D}(\varepsilon)$ (B) defined in the text. The uniaxial stretching of the elastic ECM generated the effective strains map shown in (C). Mechanically biased random cell motion is clearly observed in (B). In (C), the iso-levels of cell density have been superimposed to the effective strains map (see Appendix D). In (A) and (B), scales correspond to normalized cell density.

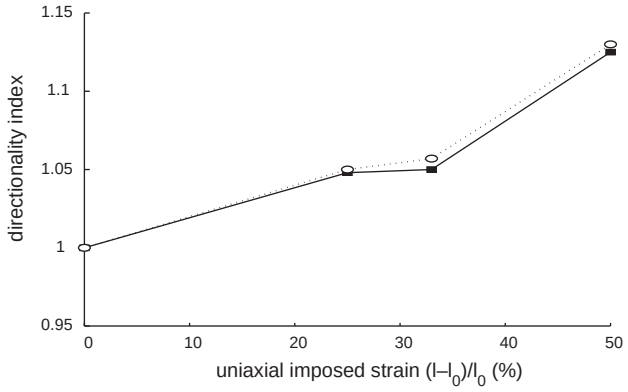

Fig. 5. Comparison between experimental and theoretical directionality indexes in mechanically biased cell migration for increasing uniaxial stretching of the ECM. Solid squares: experimental index reported by Korff and Augustin (1999) from cell migration experiments on pre-strained fibrin gels. Open circles: theoretical index derived from closed iso-contour curves (Fig. 4C). l_0 and l are the initial and deformed length of the sample, respectively.

concentration which has to be seeded initially in order to observe lacunae formation: for low EC density, the cellular traction is too weak to initiate tubulogenesis. Conversely, for high cell density, the inhibition contact phenomenon prevents the amplification of local mechanical stresses induced by cell traction forces. In order to get a measurement of the cell network extension and associated ECM remodeling, we simulated our model with increasing values of the amount of EC seeded onto the ECM. These values were taken in the experimental range analysed in Vailhe et al. (1997). We then computed from our simulations the integral $\int_\Omega \delta(\rho(x,y) > 1)\,\mathrm{d}s$, where $\delta(.) = 1$ if the condition on the local ECM density is satisfied, zero otherwise. This estimator gives an indication of the percentage of lacunae network, similarly to the experimental network one used in Vailhe et al. (1997). Fig. 9 shows that our numerical simulations of the ECM remodeling are in good agreement with the theoretical instability predictions and experimental results: the mechanical forces triggering the tubulogenesis process cannot develop if the number of seeded EC is either too small or too large (Table 3).

Interestingly, we also show in Fig. 10 that the variation of initial EC concentration for different values of the total amount of seeded cells, initially distributed in a quasi-homogeneous (slightly randomly perturbed) manner in space, give rise to many different cell network patterns (Fig. 10). (B) exhibits isolated cords of cells, while (C) mimics the formation of anastomoses recurrently observed during angiogenesis. However, it is only in (D) that a cell network above a percolation threshold (Gamba et al., 2003) is observed: this latter spatial organization would correspond to a functional capillary-like network, where fluid exchange would be possible from one domain boundary to the opposite one. Globally, these simulations provide some

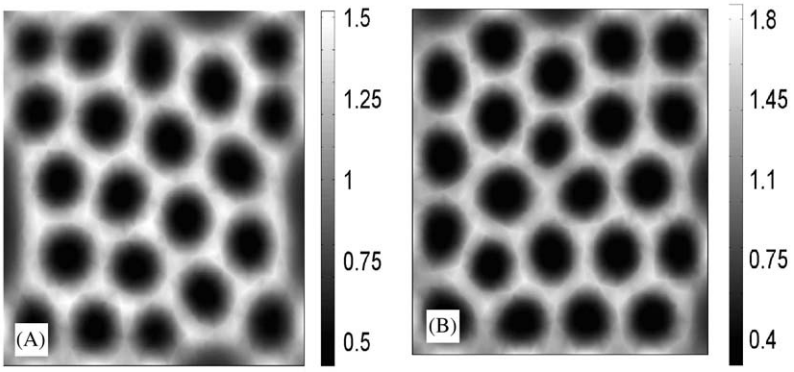

Fig. 6. EC networks simulated, with our model, in the case of isotropic diffusion with coefficient D_0 (A) or when considering strain-dependent cell diffusion (B). At the steady state, cell network patterns are almost the same. Parameters are those used in Fig. 3. Scales correspond to the normalized EC density.

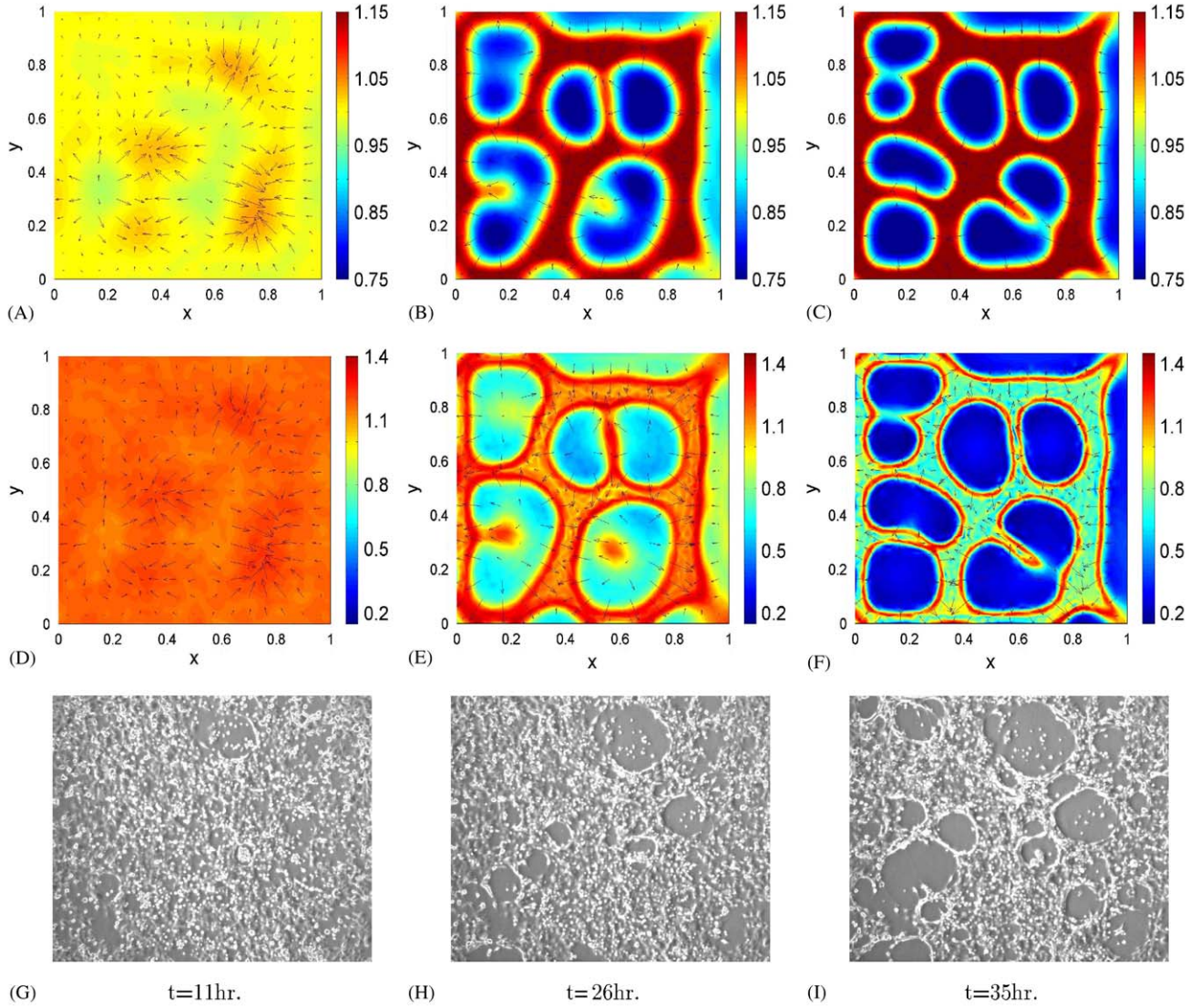

Fig. 7. Comparison between simulated (A–C) and observed (G–I) morphologies of the EC–ECM composite medium at successive times ($t1 = 11$ h, $t2 = 26$ h, $t3 = 35$ h) of the tubulogenesis process. At each time, the map of the corresponding von Mises stresses σ_{vm} (see Appendix D) in the ECM is presented (D–F). The superimposed arrows indicate direction and amplitude of the local displacement vector, the arrow length being proportional to the vector norm. First, cells aggregate (A), then lacunae appear (B). Finally, lacunae network becomes well defined (C). Arrows exhibit the ECM displacement and accumulation towards the borders of the lacunae, in pace with increasing values of the ECM stresses. Normalized parameters for this simulation are: $\tau = 1.35$, $\lambda = 0.15$, $\mu = 0.49$, $\mu_1 = \mu_2 = 0.03$, $\beta_1 = \beta_2 = 0.003$, $D_0 = 4 \times 10^{-5}$, $h = 4 \times 10^{-4}$, $N_2 = 2.5$, $s = 200$. (A–C) scales correspond to normalized ECM density, (D–F) scales to the von Mises stresses distribution.

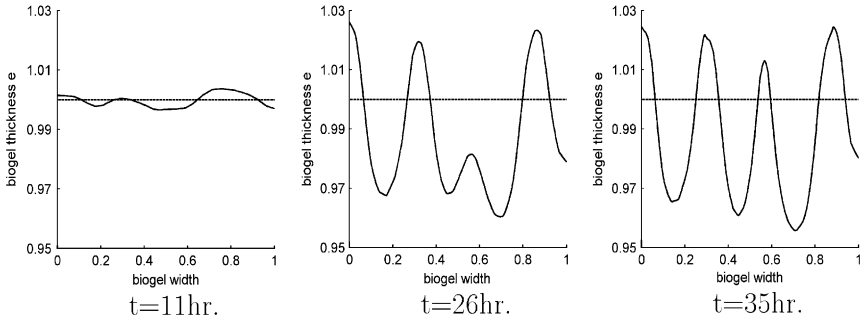

Fig. 8. Progressive amplification of the lacunae depth simulated with the mechanical model. Variations of the thickness of an ECM cross-section taken along the line $y = 0.7$ (Fig. 7) are presented at successive times $t = 11$, 26 and 35 h. As time goes on, lacunae become deeper and irregularly distributed.

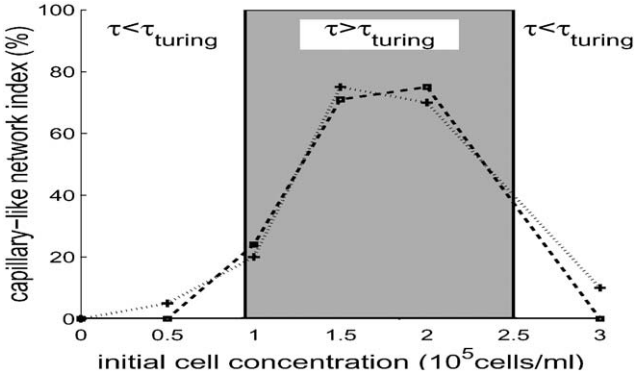

Fig. 9. Influence of the EC seeded concentration on the cell network formation. Grey area: theoretical instability window derived from linear stability analysis, dotted line: experimental cellular network index reported by Vailhe et al. (1997), dashed line: cellular network index computed from the model simulations. A very good agreement is obtained between experimental results, bifurcation analysis and model simulations. Normalized parameters used were: $\tau = 1.53 \times 10^{-11} n_0^2$, $\lambda = 1.54$, $\mu = 2.31$, $\mu_1 = \mu_2 = 0.308$, $\beta_1 = \beta_2 = 0.0001$, $N_2 = 6.58 \times 10^5/n_0$, $D_0 = 4 \times 10^{-7}$, $h = 4 \times 10^{-6}$, $s = 800$.

theoretical guidelines for understanding how further control of cell proliferation, leading to increased values of the net amount of endothelial cells, could modify the functionality of the cell network arising from the tubulogenesis process.

6.2.2. Critical threshold for fibrin concentrations

A numerical approach, similar to the one described in the previous paragraph, has been used to analyse the influence of initial ECM density on tubulogenesis. Indeed, fibrin concentration is a critical parameter in in vitro angiogenesis experiments (Vailhe et al., 1997, 1998), since it affects the biogel stiffness. Similar results are obtained when the stiffness of other extracellular matrices such as type-I collagen or Matrigel (Deroanne et al., 2001) is modified. We took benefit of previous experiments and modeling of fibrin gels rheology (Benkherourou et al., 2000) to get estimated values of the fibrin gels Young's modulus E, for the experimental range of fibrin concentrations considered in our simulations. Accordingly, we can compute the bifurcation curve corresponding to the critical cellular traction amplitude τ_{turing} when ECM density varies. As in the previous paragraph, we measure the network index, associated with each ECM remodeling pattern, thanks to the quantity $\int_\Omega \delta(\rho > 1)\,\mathrm{d}s$. Comparison between theoretical values and experimental index values reported in Vailhe et al. (1997) are summarized in Fig. 11. The prediction of the range of fibrin concentrations, for which tubulogenesis occurs, is quite accurate and correspond to experimental values (Table 3).

6.2.3. Influence of increasing matrix thickness

In the previous sections, we investigated the influence of intrinsic model parameters, defining either EC–ECM mechanical interactions or cell migratory behavior. We analyse here the influence of external parameters such as those defined by the boundary conditions imposed on the ECM. It is known that these boundary conditions can dramatically modify the cell mechanical behavior, as exemplified for instance in the compaction of collagen gels by cells: significant cell spreading and cell traction forces are observed when the matrix boundaries are fixed, contrary to the situation where ECM boundaries are free to move (Shreiber et al., 2001). We study here if the attachment the ECM to the bottom of the Petri dish can significantly change the dynamics and the morphology of ECM remodeling. This is indeed a way for controlling the ECM mechanical response to cell traction stresses, intrinsic values of the ECM elasticity moduli being given. According to our model formulation, the additional shear stresses induced by this boundary effect are taken into account by an elastic restoring body force, whose amplitude decreases with increasing ECM thickness. The validation of this formulation is carried out with reference to the experimental work of Vernon et al. (1992), which reported the influence of gradients of ECM thickness on the formation of cellular networks.

Table 3
Quantitative comparison of critical parameters between experimental data (Vailhe et al., 1997) and theoretical results

Critical parameter	Units	Theoretical value	Exp. value	Fig.
n_0 (appearance of lacunae)	cell/cm^3	0.95×10^5	$0.5 \times 10^5 < \cdots < 10^5$	9
n_0 (disappearance of lacunae)	cell/cm^3	2.5×10^5	$2 \times 10^5 < \cdots < 3 \times 10^5$	9
ρ_0 (disappearance of lacunae)	mg/cm^3	1.35	$1 < \cdots < 1.5$	11

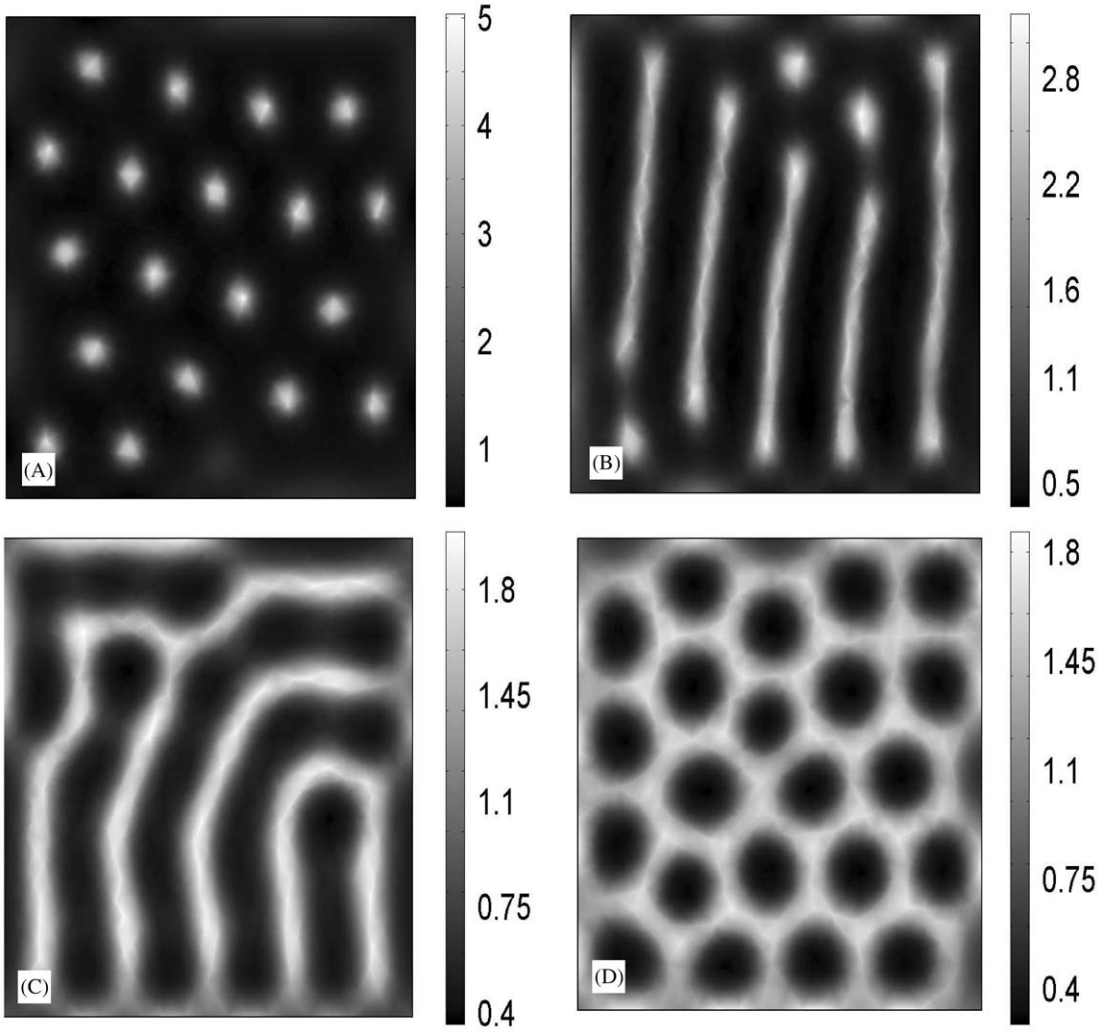

Fig. 10. Steady-state EC cellular networks obtained for different values of the initial cell concentration: (A) $n_0 = 5 \times 10^4$ cell/cm^3; (B) $n_0 = 7 \times 10^4$ cell/cm^3; (C) $n_0 = 9.5 \times 10^4$ cell/cm^3 and (D) $n_0 = 1.1 \times 10^5$ cell/cm^3. White areas denote areas of high cell densities, according to the indicated grey level chart. Parameters are those used in Fig. 3, except of those depending on n_0. (D) The EC pattern corresponds to the mode (9,5). Scales correspond to normalized EC density.

As in Vernon et al. (1992), we have considered two gradients of ECM thickness: the first one with a 8% slope over a rectangular 3.75 mm × 1.5 mm domain, the second one with a 2% slope on a longer 15 mm × 1.5 mm rectangle. The simulated spatial organization of the cellular networks corresponding to both thickness gradients are shown in (Fig. 12A and B) together with the experimental cellular networks obtained by Vernon et al. (1992) for bovine aortic cells cultured on basement membrane matrix with a thickness gradient of 2.8% (Fig. 12C). These simulated cellular spatial organization reproduced quite well the experimental observations of Vernon et al. (1992): (i) lacunae are more numerous and larger in area where the ECM is thicker, (ii) the transition from quasi-homogeneous distribution of cells at the ECM surface (left) to cellular networks (right)

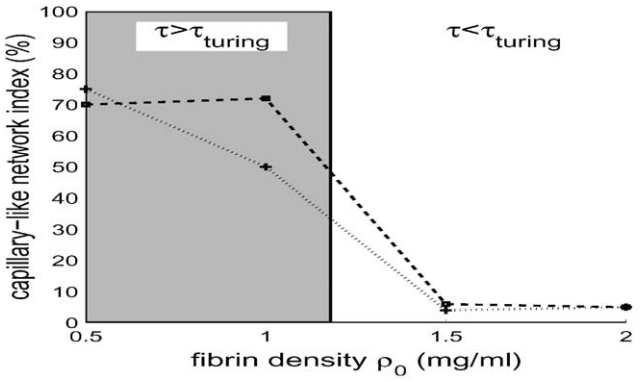

Fig. 11. Influence of the fibrin gel concentration, and thus of the gel stiffness, on the EC network formation. Grey area: theoretical instability window derived from linear stability analysis, dotted line: experimental cellular network index reported by Vailhe et al. (1997), dashed line: cellular network index computed from the model simulations. As in Fig. 9, a very good agreement between numerical simulations and experimental results is obtained. Normalized parameters are: $\tau = 1.3$, $\lambda = 115,740\rho_0^2$, $\mu = 231,480\rho_0^2$, $\mu_1 = \mu_2 = 154\rho_0$, $h = 0.04\rho_0$, $\beta_1 = \beta_2 = 0.003$, $D_0 = 8 \times 10^{-6}$, $N_2 = 2.5$, $s = 8800$.

occurs more abruptly when EC are seeded on a stiffer ECM gradient (Fig. 12A).

7. Discussion

The development of vascular structures is of fundamental importance in physio-pathological developmental processes. In vitro angiogenesis assays provide a simplified but controlled experimental framework within which the complexity of the cell–extracellular matrix interactions can be analysed (Folkman and Haudenschild, 1980; Ingber, 2002). They predominantly reveal the self-organizing properties of EC which can rearrange in tubular structures when they are seeded on ECM with appropriated mechanical properties (Vernon et al., 1992; Vailhe et al., 2001). However, understanding the appearance and regulation of such cellular spatial structures in the experimental framework presented here necessarily implies to consider both cell migration and cellular mechanical stresses. They are the core of the instability driven process of the cell network formation

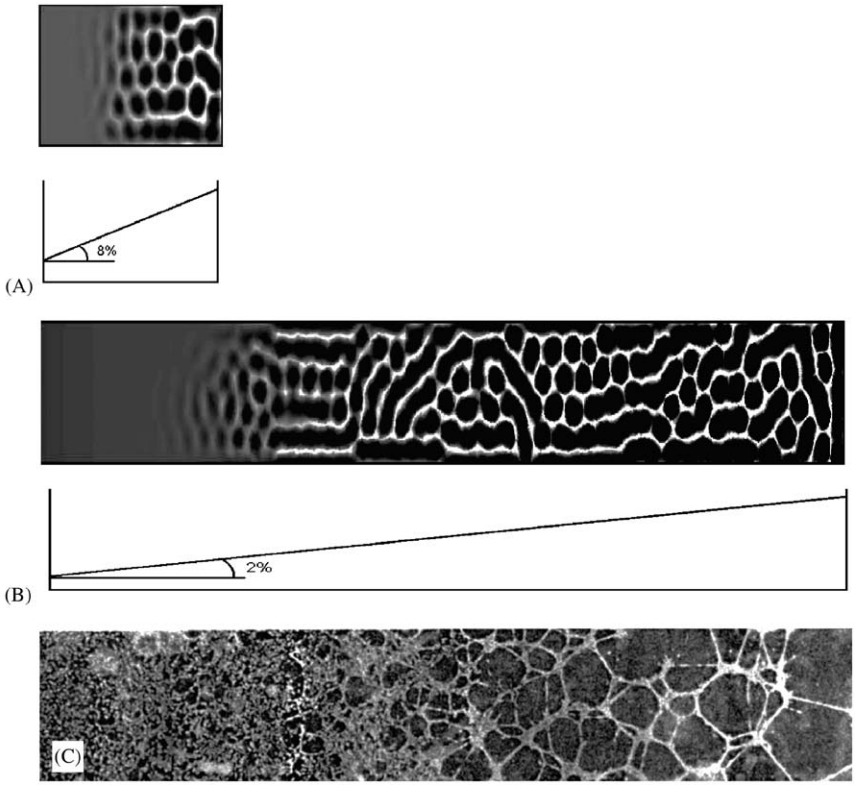

Fig. 12. Influence of gradients of ECM thickness on the observed morphologies of the cellular network and lacunae spatial distribution. Both a weak (2%) and a stiffer (8%) gradients have been considered to compare with the experimental results obtained by Vernon et al. (1992). The ECM is thinner on the left side than on the right side. (A, B) The formation of lacunae in the thickest regions of the ECM is enhanced. White areas correspond to high ECM (or EC) density, while ECM (or EC) densities are low in black areas. Transition from flattened shape to well-defined networks (corresponding to deeper lacunae) is more abrupt for stiffer gradients (A). Both simulations compared quite well with the experimental planar matrix morphologies reported in Vernon et al. (1992) for the same gradients of matrix thickness. For comparison, the experimental morphology obtained for the lowest gradient is shown (C), adapted from (Vernon et al., 1992). Normalized parameters for these simulations are: $\tau = 2.82$, $\lambda = 0.15$, $\mu = 0.23$, $\mu_1 = \mu_2 = 0.3$, $\beta_1 = \beta_2 = 0.01$, $D_0 = 8 \times 10^{-6}$, $h = 4 \times 10^{-4}$, $N_2 = 3$, $s = 8800$.

observed when EC are cultured in vitro on various extracellular matrices with given thickness and in absence of exogenous source of chemoattractants. Thus, the chemotactic scenario alone cannot explain this morphogenetic process and theoretical models, different from those recently proposed (Gamba et al., 2003; Serini et al., 2003), are required.

In close connection with experiments performed on fibrin gels with different endothelial cells (HUVEC, EAhy926 cells) (Vailhe et al., 1997, 1998), we analysed in this paper the fine tuning that exists between cell traction forces and the mechanical resistance of the ECM. Indeed, the bifurcation diagrams, derived from our model, are known to be valuable tools for predicting the threshold values and range of experimental variables within which lacunae and theoretical tubulogenesis can take place. Considering both these so defined instability domains and parameter values derived from previous experiments (Ferrenq et al., 1997; Benkherourou et al., 2000), we simulated the emergence of lacunae 10 h after EC seeding, with a clearly visible rearrangement of cells into tube-like structures (Fig. 7). We have shown that haptotaxis enabled the creation of endothelial tube networks for larger values of the Young's modulus than those considered in Manoussaki et al. (1996) and in Murray (2003b). Thus, active cell migration appears as a way to increase the "reactivity" of the EC–ECM composite medium to the tubulogenesis process. Conversely, a decrease of haptotatic cell motion, for example through a decreasing affinity of cell receptors to ECM adhesive proteins, would require an increasing active cell contractility and mechanical efficiency of the cytoskeleton to overcome reduced migration.

The model also explains nicely how ECM remodeling is controlled both by the seeded EC concentration (Fig. 9), where too low or too high cell density strongly hampers cell network formation, and by fibrin gel concentration (Fig. 11). The model simulations also account for the original experiments of Vernon et al. (1992), conducted on ECM with increasing thickness. Indeed, we simulated increased cell network formation when going from the thinner to the thicker part of the matrix (Fig. 12). Let us remark that, formally, our theoretical approach shares some similarities with the work of Painter (2000), which analysed the influence on pattern formation of a biochemical parameter whose value changes with the domain thickness. However, in our case, the influence of medium thickness corresponds to a boundary condition effect, all model parameters being unchanged.

A fundamental implication of cell traction forces is that EC can remodel the surrounding ECM through the reorganization of its structure by creating tension lines and structural pathways which can provide migration cues for other cells. Simulation of such strain-induced anisotropic cell diffusion was investigated in this paper, but the strain amplitude appears to be too weak to influence qualitatively the lacunae network pattern formation. Similar conclusions were found by Manoussaki et al. (1996) and by Murray et al. (1998), Murray (2003b) even in absence of haptotactic cell migration.

As a whole, the combined experimental–theoretical approach presented here details the role of different experimental parameters within an integrated description of cell–ECM interactions, and successfully explains the first stages of the lacunae formation within the biogel. Different limitations of the model can be however noticed: the constitutive stress–strain relationships are formulated in the limit of the small strain formulation, and our reduced analysis of the tubulogenesis in a 2D domain do not take into account the vertical cellular stresses which will occur as soon as cells migrate within the ECM. However, we think that the continuous mechanical approach developed here is quite appropriated for an extended incorporation of new experimental factors, and refined analysis of the different signal transduction pathways involved in cell proliferation, matrix proteolysis and growth factor secretion, which are influenced by the biomechanical context.

Acknowledgements

We thank Caroline Rosello and Jocelyne Clément-Lacroix for their contributions to the in vitro experiments. This work was supported by a grant ACI Télémédecine from French Ministère de la Recherche, de la Science et de la Technologie.

Appendix A. Relationship between ECM thickness and ECM density

Thanks to the Hooke's law, and assuming that all strain tensor component are only spatially dependent on x and y, we can deduce that all stress tensor components are only dependent on x and y. Moreover, we have

$$\sigma_{33}^{hooke}(x,y,t) = \frac{E}{1+v}\,\varepsilon_{33}(x,y,t) + \frac{Ev}{(1+v)(1-2v)}\,\theta_{3D}(x,y,t),$$

where $\theta_{3D}(x,y,t) = \frac{\partial u_1(x,y,z,t)}{\partial x} + \frac{\partial u_2(x,y,z,t)}{\partial y} + \frac{\partial u_3(x,y,z,t)}{\partial z}$ and $u_i(x,y,z,t)$ are the components of the displacement vector $\mathbf{u}(x,y,z,t)$. Assuming furthermore that the vertical stress component is negligible ($\sigma_{33}^{hooke}(x,y,t) = 0$), we obtain

$$\varepsilon_{33}(x,y,t) = -\frac{v}{1-2v}\,\theta_{3D}(x,y,t). \tag{A.1}$$

Thanks to the local mass conservation of ECM, we can write that $\rho\,\mathrm{d}V = \rho_0\,\mathrm{d}V_0$, where $\mathrm{d}V_0$ and $\mathrm{d}V$, ρ_0 and ρ, are the elementary volumes, densities at the initial and deformed state, respectively. Knowing that $\mathrm{d}V = \mathrm{d}X^1\,\mathrm{d}X^2\,\mathrm{d}X^3$, $\mathrm{d}V_0 = \mathrm{d}X_0^1\,\mathrm{d}X_0^2\,\mathrm{d}X_0^3$, where $\mathrm{d}X_0^1$, $\mathrm{d}X_0^2$,

dX_0^3 and dX^1, dX^2, dX^3 are dimensions of volumes dV_0 and dV, respectively, and by writing that $dX^i = (1 + \varepsilon_{ii})\, dX_0^i$ for each $i = 1 \ldots 3$, we obtain, under the small strain hypothesis

$$\rho(x, y, t) = \rho_0(1 - \theta_{3D}(x, y, t)). \tag{A.2}$$

The thickness is calculated by using $e(x, y, t) = e_0(x, y)(1 + \varepsilon_{33})$, where $e_0(x, y)$ is the initial ECM thickness. Combining this expression of $e(x, y, t)$ with Eqs. (A.1) and (A.2), we get formula (5).

Appendix B. Non-dimensionalization of the model variables

The mechanocellular model equations can be non-dimensionalized by re-scaling time with the characteristic time-scale T (hours), the typical size L (diameter of the Petri dish) of the domain Ω, the initial EC concentration n_0 and the initial fibrin density ρ_0. We set

$$\rho^* = \frac{\rho}{\rho_0}, \quad n^* = \frac{n}{n_0}, \quad u_1^* = \frac{u_1}{L}, \quad u_2^* = \frac{u_2}{L}, \quad x^* = \frac{x}{L},$$
$$y^* = \frac{y}{L}, \quad t^* = \frac{t}{T}$$

with the normalized parameters:

$$D_0^* = \frac{D_0 T}{L^2}, \quad \mu_1^* = \frac{\mu_1 \rho_0}{L^2 T}, \quad \mu_2^* = \frac{\mu_2 \rho_0}{L^2 T}, \quad N_2 = \frac{N_2}{n_0},$$
$$h^* = \frac{hT\rho_0}{L^2}, \quad \beta_1^* = \frac{\beta_1}{L^2}, \quad \beta_2^* = \frac{\beta_2}{L^2}$$
$$\lambda^* = \frac{E\nu\rho_0}{L^2(1+\nu)(1-2\nu)}, \quad \mu^* = \frac{E\rho_0}{2(1+\nu)L^2},$$
$$\tau^* = \frac{\tau\rho_0^2 n_0^2}{L^2}. \tag{B.1}$$

In the following text, asterisks have been dropped for convenience. The non-dimensionalized model is then

$$\nabla.[2\mu(\boldsymbol{\varepsilon} - \beta_1\nabla^2\boldsymbol{\varepsilon}) + \lambda(\theta - \beta_2\nabla^2\theta)\,\mathbf{Id} + \mu_1\frac{\partial \boldsymbol{\varepsilon}}{\partial t} + \mu_2\frac{\partial \theta}{\partial t}\mathbf{Id} + \tau\rho n(N_2 - n)\,\mathbf{Id}] = s\frac{\mathbf{u}}{\rho},$$
$$\frac{\partial n}{\partial t} + \nabla.\left[-\nabla.(\mathbf{D}(\boldsymbol{\varepsilon})n) + hn\nabla\rho + n\frac{\partial \mathbf{u}}{\partial t}\right] = 0,$$
$$\frac{\partial \rho}{\partial t} + \nabla.\left[\rho\frac{\partial \mathbf{u}}{\partial t}\right] = 0. \tag{B.2}$$

Appendix C. Linear stability analysis

The linearized system associated to the nonlinear partial differential system (B.2) is

$$\nabla.\left[2\mu(\boldsymbol{\varepsilon} - \beta_1\nabla^2\boldsymbol{\varepsilon}) + \lambda(\theta - \beta_2\nabla^2\theta)\mathbf{Id} + \mu_1\frac{\partial \boldsymbol{\varepsilon}}{\partial t} + \mu_2\frac{\partial \theta}{\partial t}\mathbf{Id} + \tau n(N_2 - 2)\mathbf{Id} + \tau\rho(N_2 - 1)\mathbf{Id}\right] - s\mathbf{u} = 0,$$
$$\frac{\partial n}{\partial t} + \nabla.\left[-D_0\nabla n - \frac{D_0}{2}\nabla^2\mathbf{u} + h\nabla\rho + \frac{\partial \mathbf{u}}{\partial t}\right] = 0,$$
$$\frac{\partial \rho}{\partial t} + \nabla.\left[\frac{\partial \mathbf{u}}{\partial t}\right] = 0.$$

The eigenvalue ξ_1, used in the dispersion relationship (9), is equal to $-2(\mu\beta_1 r^2 + s + \mu r)/\mu_1 r$. Therefore, the real part of ξ_1 is always negative. The coefficients $a(r)$, $b(r)$ and $c(r)$, used in the dispersion relationship (9), are

$$a(r) = r(\mu_1 + \mu_2),$$

$$b(r) = (D_0(\mu_1 + \mu_2) + 2\mu\beta_1 + \lambda\beta_2)r^2 + (2\mu + \lambda + \tau(3 - 2N_2))r + s,$$

$$c(r) = D_0(2\mu\beta_1 + \lambda\beta_2)r^3 + \left(D_0(2\mu + \lambda) + \tau\left(h\left(2 - N_2\right) + D_0\left(2 - \frac{3N_2}{2}\right)\right)\right)r^2 + D_0 sr.$$

Appendix D. Formulae for the von Mises stress σ_{vm} and for the effective strain e_{ff}

The von Mises stress σ_{vm} is defined by

$$\sigma_{vm} = \sqrt{\frac{3}{2}\sum_{i,j} S_{ij}^2},$$

where S_{ij} are the components of the deviatoric stress tensor. They are defined as follows:

$$S_{ij} = \sigma_{ij} - \frac{1}{3}Tr(\boldsymbol{\sigma})\delta_{ij},$$

where $\boldsymbol{\sigma} = \boldsymbol{\sigma}_{cell} + \boldsymbol{\sigma}_{ecm}$, Tr is the trace operator and δ_{ij} is the Kronecker symbol ($\delta_{ij} = 1$ if $i = j$, 0 otherwise).

In a similar way, the effective strain e_{ff} is defined by

$$e_{ff} = \sqrt{\frac{2}{3}\sum_{i,j} e_{ij}^2},$$

where e_{ij} are the components of the deviatoric strain tensor. They are defined as follows:

$$e_{ij} = \varepsilon_{ij} - \frac{1}{3}Tr(\boldsymbol{\varepsilon})\delta_{ij},$$

where $\boldsymbol{\varepsilon}$ is the strain tensor.

References

Anderson, A.R.A., Chaplain, M.A.J., 1998. Continuous and discrete mathematical models of tumor-induced angiogenesis. Bull. Math. Biol. 60, 857–900 doi: 10.1006/bulm.1998.0042.

Balaban, N.Q., Schwarz, U.S., Riveline, D., Goichberg, P., Tzur, G., Sabanay, I., Mahalu, D., Safran, S., Bershadsky, A., Addadi, L., Geiger, B., 2001. Force and focal adhesion assembly: a close relationship studied using elastic micropatterned substrates. Nat. Cell Biol. 3, 466–472.

Barocas, V.H., Tranquillo, R.T., 1997. An anisotropic biphasic theory of tissue-equivalent mechanics: the interplay among cell traction,

fibrillar network deformation, fibril alignment, and cell contact guidance. J. Biomech. Eng. 119, 137–145.

Barocas, V.H., Moon, A.G., Tranquillo, R.T., 1995. The fibroblast-populated collagen microsphere assay of cell traction force—Part 2: measurement of the cell traction parameter. J. Biomech. Eng. 117, 161–170.

Benkherourou, M., Gumery, P.Y., Tranqui, L., Tracqui, P., 2000. Quantification and macroscopic modeling of the nonlinear viscoelastic behavior of strained gels with varying fibrin concentrations. IEEE Trans. Biomed. Eng. 47, 1465–1475.

Cines, D.B., Pollak, E.S., Buck, C.A., Loscalzo, J., Zimmerman, G.A., McEver, R.P., Pober, J.S., Wick, T.M., Konkle, B.A., Schwartz, B.S., Barnathan, E.S., McCrae, K.R., Hug, B.A., Schmidt, A.M., Stern, D.M., 1998. Endothelial cells in physiology and in the pathophysiology of vascular disorders. Blood 91, 3527–3561.

Cook, J., 1995. Mathematical models for dermal wound healing: wound contraction and scar formation. Ph.D. Thesis, University of Washington, Seattle, pp. 98–133.

Cruywagen, G.C., Maini, P.K., Murray, J.D., 1994. Travelling waves in a tissue interaction model for skin pattern formation. J. Math. Biol. 33, 193–210.

Cruywagen, G.C., Maini, P.K., Murray, J.D., 1997. Biological pattern formation on two-dimensional spatial domains: a nonlinear bifurcation analysis. SIAM J. Appl. Math. 57, 1485–1509.

Delvoye, P., Wiliquet, P., Leveque, J.L., Nusgens, B.V., Lapiere, C.M., 1991. Measurement of mechanical forces generated by skin fibroblasts embedded in a three-dimensional collagen gel. J. Invest. Dermatol. 97, 898–902.

Deroanne, C.F., Lapiere, C.M., Nusgens, B.V., 2001. In vitro tubulogenesis of endothelial cells by relaxation of the coupling extracellular matrix-cytoskeleton. Cardiovasc. Res. 49, 647–658.

Dickinson, R.B., Tranquillo, R.T., 1993. A stochastic model for adhesion-mediated cell random motility and haptotaxis. J. Math. Biol. 31, 563–600.

DiMilla, P.A., Quinn, J.A., Albelda, S.M., Lauffenburger, D.A., 1992. Measurement of individual cell migration parameters for human tissue cells. AIChE J. 38, 1092–1104.

Ferrenq, I., Tranqui, L., Vailhe, B., Gumery, P.Y., Tracqui, P., 1997. Modelling biological gel contraction by cells: mechanocellular formulation and cell traction force quantification. Acta Biotheor. 45, 267–293.

Folkman, J., Haudenschild, C., 1980. Angiogenesis in vitro. Nature (London) 288, 551–556.

Fung, Y.C., 1993. Biomechanics. Mechanical Properties of Living Tissues, 2nd Edition. Springer: New York, pp. 50–52.

Gamba, A., Ambrosi, D., Coniglio, A., de Candia, A., Di Talia, S., Giraudo, E., Serini, G., Preziosi, L., Bussolino, F., 2003. Percolation, morphogenesis and burgers dynamics in blood vessels formation. Phys. Rev. Lett. 90, 118101–1–118101–4.

Gerhardt, H., Golding, M., Fruttiger, M., Ruhrberg, C., Lundkvist, A., Abramsson, A., Jeltsch, M., Mitchell, C., Alitalo, K., Shima, D., Betsholtz, C., 2003. VEGF guides angiogenic sprouting utilizing endothelial tip cell filopodia. J. Cell Biol. 161, 1163–1177.

Girton, T.S., Barocas, V.H., Tranquillo, R.T., 2002. Confined compression of a tissue-equivalent: collagen fibril and cell alignment in response to anisotropic strain. J. Biomech. Eng. 124, 568–575.

Grassl, E.D., Oegema, T.R., Tranquillo, R.T., 2002. Fibrin as an alternative biopolymer to type-I collagen for the fabrication of a media equivalent. J. Biomed. Mater. Res. 60, 607–612 doi: 10.1002/jbm.10107.

Hayen, W., Goebeler, M., Kumar, S., Riessen, R., Nehls, V., 1999. Hyaluronan stimulates tumor cell migration by modulating the fibrin fiber architecture. J. Cell Sci. 112, 2241–2251.

Holmes, M.J., Sleeman, B.D., 2000. A mathematical model of tumour angiogenesis incorporating cellular traction and viscoelastic effects. J. Theor. Biol. 202, 95–112 doi: 10.1006/jtbi.1999.1038.

Ingber, D.E., 2002. Mechanical signaling and the cellular response to extracellular matrix in angiogenesis and cardiovascular physiology. Circ. Res. 91, 877–887.

Jamora, C., Fuchs, E., 2002. Intercellular adhesion, signalling and the cytoskeleton. Nature Cell Biol. 4, E101–108 doi: 10.1038/ncb0402-e101.

Korff, T., Augustin, H.G., 1999. Tensional forces in fibrillar extracellular matrices control directional capillary sprouting. J. Cell Sci. 112, 3249–3258.

Lambert, C.A., Colige, A.C., Lapiere, C.M., Nusgens, B.V., 2001. Coordinated regulation of procollagens I and III and their post-translational enzymes by dissipation of mechanical tension in human dermal fibroblasts. Eur. J. Cell. Biol. 80, 479–485.

Levine, H.A., Sleeman, B.D., Nilsen-Hamilton, M., 2001. Mathematical modeling of the onset of capillary formation initiating angiogenesis. J. Math. Biol. 42, 195–238 doi: 10.1007/s002850000037.

Maheshwari, G., Lauffenburger, D.A., 1998. Deconstructing (and reconstructing) cell migration. Microsc. Res. Tech. 43, 358–368.

Manoussaki, D., Lubkin, S.R., Vernon, R., Murray, J.D., 1996. A mechanical model for the formation of vascular networks in vitro. Acta Biotheor. 44, 271–282.

Moon, A.G., Tranquillo, R.T., 1993. Fibroblast-populated collagen microsphere assay of cell traction force: Part 1. continuum model. AIChE J. 39, 163–175.

Murray, J.D., 2003a. Mechanical theory for generating pattern and form. In: Murray, J.D. (Ed.), Mathematical Biology II: Spatial Models and Biomedical Applications, 3rd Edition. Springer, New York, pp. 311–334.

Murray, J.D., 2003b. A mechanical theory for vascular network formation. In: Murray, J.D. (Ed.), Mathematical Biology II: Spatial Models and Biomedical Applications, 3rd Edition. Springer, New York, pp. 416–440.

Murray, J.D., Oster, G.F., 1984. Cell traction models for generating pattern and form in morphogenesis. J. Math. Biol. 19, 265–279.

Murray, J.D., Manoussaki, D., Lubkin, S.R., Vernon, R., 1998. A mechanical theory of in vitro vascular network formation. In: Little, C.D., Mironov, V., Sage, E.H. (Eds.), Vascular Morphogenesis: In Vivo, In Vitro, In Mente. Birkhäuser, Boston, Basel, Berlin, pp. 173–188.

Olsen, L., Maini, P.K., Sherratt, J.A., 1998. Spatially varying equilibria of mechanical models: application to dermal wound contraction. Math. Biosci. 147, 113–129 doi: 10.1016/S0025-5564(97)00075-8.

Othmer, H.G., Stevens, A., 1997. Aggregation, blowup and collapse: the abc's of taxis in reinforced random walks. SIAM J. Appl. Math. 57, 1044–1081.

Painter, K.J., 2000. Modelling of pigment pattern formation in the skin of fishes. In: Maini, P.K., Othmer, H.G. (Eds.), Mathematical Models for Biological Pattern Formation. Springer, Berlin/Heidelberg, pp. 59–82.

Palecek, S.P., Loftus, J.C., Ginsberg, M.H., Lauffenburger, D.A., Horwitz, A.F., 1997. Integrin–ligand binding properties govern cell migration speed through cell-substratum adhesiveness. Nature (London) 385, 537–540.

Perumpanani, A.J., Byrne, H.M., 1999. Extracellular matrix concentration exerts selection pressure on invasive cells. Eur. J. Cancer 35, 1274–1280.

Piechor, K., Kazmierczak, B., 2002. Heteroclinic solutions for a model of skin morphogenesis. In: Capasso, V. (Ed.), Mathematical Modelling & Computing in Biology and Medicine. Fifth ESMTB Conference 2002, Esculapio, Milan, pp. 545–551.

Roman, B.L., Weinstein, B.M., 2000. Building the vertebrate vasculature: research is going swimmingly. Bioessays 22, 882–893.

Sage, E.H., Vernon, R.B., 1994. Regulation of angiogenesis by extracellular matrix: the growth and the glue. J. Hypertens. Suppl. 12, S145–S152.

Scherer, G.W., Hdach, H., Phalippou, J., 1991. Thermal expansion of gels: a novel method for measuring permeability. J. Non-cryst. Solid 130, 157–170.

Serini, G., Ambrosi, D., Giraudo, E., Gamba, A., Preziosi, L., Bussolino, F., 2003. Modeling the early stages of vascular network assembly. EMBO J. 22, 1771–1779.

Sherratt, J.A., Chaplain, M.A.J., 2001. A new mathematical model for a vascular tumour growth. J. Math. Biol. 43, 291–312.

Sherratt, J.A., Sage, E.H., Murray, J.D., 1993. Chemical control of eukaryotic cell movement: a new model. J. Theor. Biol. 162, 23–40 doi: 10.1006/jtbi.1993.1074.

Shreiber, D.I., Enever, P.A.J., Tranquillo, R.T., 2001. Effects of PDGFBB on rat dermal fibroblast behavior in mechanically stressed and unstressed collagen and fibrin gels. Exp. Cell Res. 266, 155–166.

Shreiber, D.I., Barocas, V.H., Tranquillo, R.T., 2003. Temporal variations in cell migration and traction during fibroblast-mediated gel compaction. Biophys. J. 84, 4102–4114.

Tranqui, L., Tracqui, P., 2000. Mechanical signalling and angiogenesis. The integration of cell–extracellular matrix couplings. C. R. Acad. Sci. 323, 31–47 doi: 10.1016/S0764-4469(00)00110-4.

Tranquillo, R.T., Durrani, M.A., Moon, A.G., 1992. Tissue engineering science: consequences of cell traction force. Cytotechnology 10, 225–250.

Vailhe, B., Ronot, X., Tracqui, P., Usson, Y., Tranqui, L., 1997. In vitro angiogenesis is modulated by the mechanical properties of fibrin gels and is related to $\alpha_v\beta_3$ integrin localization. In Vitro Cell Dev. Biol. Anim. 33, 763–773.

Vailhe, B., Lecomte, M., Wiernsperger, N., Tranqui, L., 1998. The formation of tubular structures by endothelial cells is under the control of fibrinolysis and mechanical factors. Angiogenesis 2, 331–344.

Vailhe, B., Vittet, D., Feige, J.-J., 2001. In vitro models of vasculogenesis and angiogenesis. Lab. Invest. 81, 439–452.

Van Hinsbergh, V.W., Collen, A., Koolwijk, P., 2001. Role of fibrin matrix in angiogenesis. Ann. N. Y. Acad. Sci. 936, 426–437.

Vernon, R.B., Angello, J.C., Iruela-Arispe, M.L., Lane, T.F., Sage, E.H., 1992. Reorganization of basement membrane matrices by cellular traction promotes the formation of cellular networks in vitro. Lab. Invest. 66, 536–547.

Vernon, R.B., Lara, S.L., Drake, C.J., Iruela-Arispe, M.L., Angello, J.C., Little, C.D., Wight, T.N., Sage, E.H., 1995. Organized type I collagen influences endothelial patterns during "spontaneous angiogenesis in vitro": planar cultures as models of vascular development. In vitro Cell Dev. Biol. 31, 120–131.

Warner, T.D., Mitchell, J.A., 2003. HIF, stretching to get control of VEGF. Clin. Sci. 105, 393–394 doi:10.1042/CS20030208.

Yoshino, H., Morita, I., Murota, S.I., Ishikawa, I., 2003. Mechanical stress induces production of angiogenic regulators in cultured human gingival and periodental ligament fibroblasts. J. Periodontal Res. 38, 405–410.